

Feasibility study of propagation-based phase-contrast X-ray lung imaging on the Imaging and Medical beamline at the Australian Synchrotron

Rhiannon P. Murrie,^{a*} Andrew W. Stevenson,^{b,c} Kaye S. Morgan,^a Andreas Fouras,^d David M. Paganin^a and Karen K. W. Siu^{a,e}

^aSchool of Physics, Monash University, Victoria 3800, Australia, ^bCSIRO Materials Science and Engineering, Private Bag 33, Clayton South, Victoria 3169, Australia, ^cAustralian Synchrotron, 800 Blackburn Road, Clayton, Victoria 3168, Australia, ^dDepartment of Mechanical and Aerospace Engineering, Monash University, Victoria 3800, Australia, and ^eMonash Biomedical Imaging, Monash University, Victoria 3800, Australia. *E-mail: rhiannon.murrie@monash.edu

Propagation-based phase-contrast X-ray imaging (PB-PCXI) using synchrotron radiation has achieved high-resolution imaging of the lungs of small animals both in real time and *in vivo*. Current studies are applying such imaging techniques to lung disease models to aid in diagnosis and treatment development. At the Australian Synchrotron, the Imaging and Medical beamline (IMBL) is well equipped for PB-PCXI, combining high flux and coherence with a beam size sufficient to image large animals, such as sheep, due to a wiggler source and source-to-sample distances of over 137 m. This study aimed to measure the capabilities of PB-PCXI on IMBL for imaging small animal lungs to study lung disease. The feasibility of combining this technique with computed tomography for three-dimensional imaging and X-ray velocimetry for studies of airflow and non-invasive lung function testing was also investigated. Detailed analysis of the role of the effective source size and sample-to-detector distance on lung image contrast was undertaken as well as phase retrieval for sample volume analysis. Results showed that PB-PCXI of lung phantoms and mouse lungs produced high-contrast images, with successful computed tomography and velocimetry also being carried out, suggesting that live animal lung imaging will also be feasible at the IMBL.

Keywords: X-ray; phase contrast; lung; propagation-based; medical imaging; velocimetry; computed tomography; Australian Synchrotron.

© 2014 International Union of Crystallography

1. Introduction

One of the limiting factors in our capability to accurately diagnose, monitor and treat human lung disease has been our inability to image the lungs and airways at high resolution in real time, *in vivo*. Conventional diagnostic X-ray imaging provides limited information due to the minimal difference in X-ray attenuation between biological soft tissues and air (Lewis *et al.*, 2005). While modern imaging techniques can provide three- and even four-dimensional data with good contrast using imaging methods such as computed tomography (CT), positron emission tomography (PET) and magnetic resonance imaging (MRI), these methods lack the temporal and spatial resolution to image the rapid motion of the lungs during normal ventilation (Kitchen *et al.*, 2008; Fouras *et al.*, 2009a, 2012; Jannasch *et al.*, 2009; Dubsky *et al.*, 2012a). Lung function testing methods such as spirometry and gas wash-out provide good temporal resolution in gaining

information about the breath cycle; however, the spatial resolution provided by these methods is poor (Voorhees *et al.*, 2005; Dubsky *et al.*, 2012a). Synchrotron studies into lung imaging by Giacomini *et al.* (1998) and Bayat *et al.* (2001) utilized a xenon contrast agent to image the lungs in three dimensions; however, both the spatial and temporal resolution could be improved and the ability to image the lungs without the use of a contrast agent is desirable. If lung imaging can be achieved with both high spatial and temporal resolution, the ability to find small areas of disease under natural ventilation conditions will be improved, which will in turn allow for earlier and more accurate diagnosis, thus improving patient prognoses. Such imaging would also afford a capacity to increase our current knowledge of lung disease and expand treatment research, as treatment effectiveness and efficiency can be monitored directly with high-resolution visualization.

Phase-contrast X-ray imaging (PCXI) has been widely employed for imaging the lungs of small animals. It can reveal

individual alveoli in mice and rabbits, where alveoli measure between 40 and 200 μm in diameter (Yagi *et al.*, 1999; Faffe *et al.*, 2002; Suzuki *et al.*, 2002; Irvin & Bates, 2003), and can be used at imaging rates compatible with natural breathing cycles (2–4 Hz) (Blackstone *et al.*, 2005; Carnibella *et al.*, 2013). PCXI has been used to reveal lungs with a spatial resolution of less than 100 μm and temporal resolution of less than 20 ms (or greater than 50 frames s^{-1}) (Kitchen *et al.*, 2008; Dubsky *et al.*, 2012a; Fouras *et al.*, 2012). Phase-contrast imaging utilizes the different refractive indices of matter to highlight material interfaces by refracting sufficiently spatially coherent incident X-rays. Given the significant difference in refractive index between tissue and air, the lungs lend themselves particularly well to propagation-based PCXI. Several methodologies can be employed to achieve PCXI of the lungs, including grating interferometry (Schleede *et al.*, 2012) and analyser-based PCXI (Lewis *et al.*, 2003); however, the simplest method is that of propagation-based PCXI (PB-PCXI) (Yagi *et al.*, 1999; Kitchen *et al.*, 2004). With sufficiently large sample-to-detector propagation distances, typically of the order of tens of centimetres to a few metres (Gureyev *et al.*, 2009; Nugent, 2010; Morgan *et al.*, 2013), variations in image intensity are produced in the form of bright–dark Fresnel fringes corresponding to the air–tissue interfaces, enhancing lung visibility (Wilkins *et al.*, 1996). Additional benefits of PCXI include reduced radiation dose when compared with conventional imaging, as PCXI utilizes the refraction of X-rays through matter rather than absorption (Arfelli *et al.*, 1998; Lewis *et al.*, 2005; Zhou & Brahme, 2008), and the ability to combine with other techniques such as CT, to create detailed three-dimensional images (Mayo *et al.*, 2003; Siu *et al.*, 2008; Beltran *et al.*, 2011), or X-ray velocimetry, to study the pathways of air flow through the complex network of airways (Dubsky *et al.*, 2011, 2012a; Fouras *et al.*, 2012). Whilst CT needs no preface for this audience, an introduction to X-ray velocimetry is given in §3.4 for those readers who are unfamiliar with the technique.

The Imaging and Medical beamline (IMBL) at the Australian Synchrotron is well suited to PB-PCXI due to its high coherence and intensity, as well as an extended beamline (source-to-sample distance of greater than 137 m) that provides a beam size of up to 400 mm \times 40 mm (W \times H) at the sample position, making the imaging of larger animals, and potentially humans, possible in the future. Here, we examine the potential of the IMBL for experiments involving lung function and disease, including enhanced diagnostic techniques and treatment development, and quantify the image quality possible. We discuss the effects of both sample-to-detector propagation distance (§2.1) and source size (§2.2) on PB-PCXI image quality. We detail image quality assessment in the case of large simple objects, such as perspex (PMMA) cylinders with diameter of the order of 1 mm, as well as the more complex speckle pattern created by the lungs. The method used for determining the source size is described (§2.2). We then detail the experimental set-up and procedures (§3), and analyse the results in relation to the effects of sample-to-detector propagation distance on image quality (§4.1), effective source size on image quality (§4.2) and the

measurements of the effective source size and the potential for photon scattering in air to affect the measured source size value and image quality (§4.3). The quality of single-image transport-of-intensity phase retrieval for volume analysis (§4.4) and the feasibility of imaging small animal lungs, such as mice and rabbits, using PB-PCXI on the IMBL are also analysed, as well as the potential combination with X-ray velocimetry (§4.5) and CT (§4.6). We then present mouse lung images obtained on the new superconducting multipole wiggler in §4.7, and conclude the results of our research in §5.

2. Factors affecting image quality

A quality image can generally be defined as one that captures important features with high contrast and sufficiently high spatial resolution. In phase-contrast imaging, resolution can be limited by numerous or wide phase-contrast fringes, or by blurring from the source size, detector or the scattering of photons. However, the definition of a good quality image is ultimately defined by the aim that motivates the image capture. For instance, resolving the thin liquid layer that lines airway surfaces, which is critical to clearing debris from the airways, requires high-resolution ($<0.5 \mu\text{m}$ pixels) high-contrast images with sufficiently strong fringes to be able to determine the liquid–tissue interface (Morgan *et al.*, 2013). For images of the lungs, high-contrast speckle generally gives high lung visibility, and hence good image quality is inferred (Kitchen *et al.*, 2004). Fewer fringes are preferable, as multiple fringes will begin to overlap neighbouring features, causing the speckle pattern to blur and contrast to decrease. Pixel sizes of 10–25 μm are routinely used for synchrotron PCXI of the lungs (Fouras *et al.*, 2012; Kitchen *et al.*, 2008; Lewis *et al.*, 2005), with the smaller pixel range capable of resolving the terminal airway structures. However, it is not necessary to resolve individual alveoli to obtain useful information about the lungs, and indeed this is impossible for the majority of the lung where many alveoli are overlaid. In X-ray velocimetry, a high-contrast speckle image enables lung movement to be tracked; however, high-resolution imaging of the speckle pattern is not necessary. Conversely, lower-resolution imaging can actually smooth noise and improve the accuracy of the velocimetry (Ng *et al.*, 2012).

There are a multitude of factors that can affect image quality in PB-PCXI. The image contrast will be affected by the mean energy and energy spectrum of the incident X-ray beam, which will dictate the absorption and phase contrast observed from the sample. The spatial resolution of the imaging system will be determined by the magnification of the system and the pixel size and effective resolution of the detector. The size of the source, source-to-sample and sample-to-detector distance will also determine the extent of penumbral blurring on the image, and hence affect the resolution. Additionally, a larger source size will reduce the coherence, thereby reducing the level of phase contrast observed.

Previous studies have shown that a beam energy in the region of the high twenties to low thirties (keV) is suitable for mouse lung imaging (Yagi *et al.*, 1999; Suzuki *et al.*, 2002;

Table 1

Summary of experimental variables for experiments performed in hutches 2B and 3B on the IMBL.

Crystal bend	Primary slit width (mm)	Hutch 2B		Hutch 3B		Magnification
		R_1 (m)	R_2 (m)	R_1 (m)	R_2 (m)	
0	2	34.1	0.25	138.5	1.00	1.01
1.5	5	34.1	0.65	138.5	2.62	1.02
2†	10†	34.1	1.00	138.5	4.03	1.03
	15	34.1	1.48	138.5	5.96	1.04

† Variable was only tested in hutch 3B.

Kitchen *et al.*, 2004). This energy range strikes a balance between sufficiently high penetration of the thorax, particularly the bones, so that absorption does not dominate the phase image, whilst still maintaining good contrast in the lung tissue. For this experiment, we chose an energy of 30 keV. The magnification of the system was essentially fixed at 1 due to the large pre-set source-to-sample distance (R_1) (Table 1). A pixel size of 6.5 μm was employed, allowing small sample details to be resolved. This required exposure times in the range 300 ms to 2 s, slightly longer than those typically used in live mouse lung imaging (Kitchen *et al.*, 2008; Fouras *et al.*, 2012). However, this allowed the lung phantoms to be imaged at a higher signal-to-noise ratio so that small changes in image quality could be observed. With the energy, magnification and source-to-sample distance fixed in this experiment due to the beamline and detector array size, and the pixel size fixed due to the highest-resolution detector available with a suitable field of view (see §3.1), we shall focus on two of the principal factors that should be considered when imaging the lungs: sample-to-detector distance (R_2) and source size. These factors are considered in §2.1 and §2.2, respectively.

2.1. Sample-to-detector propagation distance

It is well known that with an increase in the sample-to-detector propagation distance sample edges will produce intensity fringes of increased contrast (Cloetens *et al.*, 1996, 1999; Wilkins *et al.*, 1996). The angle of refraction of the incident X-ray wavefront at material boundaries is dependent on the object thickness, refractive index and the energy of the incident wave. Refraction angles of the order of 10^{-5} – 10^{-6} rad for organic compounds imaged at 10–50 keV are typical (Snigirev *et al.*, 1995). These refracted waves then interfere as they propagate through free space from the exit surface of the sample to the surface of the position-sensitive detector, and the width of the produced fringes is proportional to the distance propagated within the near-field regime (Suzuki *et al.*, 2002). Whilst this provides the benefit of increased edge visibility in the phase-contrast image, one must be careful to consider an appropriate detector pixel size in relation to the desired propagation distance or *vice versa*, to avoid under-sampling the produced fringes. One must also consider that the wavefront is slightly divergent and that photons will be subject to scattering and absorption due to the presence of a long path of air. This causes the intensity of the wavefront to

decrease with increasing sample-to-detector distance, which causes a decrease in image signal-to-noise ratio and resulting degradation of image quality. Additionally, penumbral blurring of the image due to an extended incoherent source, as discussed in more detail in §2.2, is also increased with increasing propagation distance, causing additional degradation of image quality. One must also consider the field of view seen by the detector, which will decrease slightly with a decreased propagation distance. This effect is negligible for near-plane waves at synchrotron light sources, but is an important consideration for moving forward towards PB-PCXI of the lungs on a divergent laboratory source.

2.2. Source size

2.2.1. Effect on image quality. PCXI relies on a spatially coherent wavefield, such that phase variations are minimal across the incident wavefront. This means that, when the wavefield propagates to the detector, the contrast produced from phase variations is a result of the sample and not of the source. Spatial coherence is increased with distance from the source and inversely with the size of the source. Whilst a point source provides the ideal coherence properties for maximal contrast and resolution in a PB-PCXI image, in reality all X-ray sources are of finite size. In X-ray imaging set-ups, from conventional hospital or laboratory sources through to highly brilliant synchrotron sources, often the source size (by electron beam size or collimation) is chosen to balance a sufficiently short exposure with minimal penumbral blurring. Note that this is not a rule when comparing sources: a synchrotron can produce greater flux than a conventional source, but typically has a smaller source size. Increasing source size has the advantage of providing more flux, which in turn allows for shorter exposure times, of particular benefit in live animal imaging. However, an increase in source size leads to a decrease in the degree of spatial coherence of the source, which in turn affects the degree of phase enhancement in the image (Wilkins *et al.*, 1996). The observed decrease in coherence can be described by modelling an extended source as a distributed number of independent coherent point sources. The intensity of the interference fringes produced is then modelled as the sum of the PB-PCXI fringes seen from each point source within the extended source (Paganin, 2006). Since the maximum and minimum intensities of the fringes from distinct points on the extended source will not necessarily coincide, the summation of the fringes causes a decrease in contrast compared with a perfect point source (Cloetens *et al.*, 1996). This penumbral blurring, Δ , is quantified in the equation (Weitkamp *et al.*, 2006; Ng *et al.*, 2012)

$$\Delta = \sigma_s(R_2/R_1), \quad (1)$$

where σ_s is the source size. Penumbral blurring is thus one of the defining factors of the spatial resolution of the system (Larsson *et al.*, 2013). This blurring effect can be minimized by reducing the source size, which also coincides with a reduction in the brightness of incident X-rays (for a fixed exposure time), thereby increasing the noise in the image due to a

reduced number of counts. Alternatively, reducing R_2/R_1 for a fixed source size will also limit penumbral blurring. One particular advantage of performing PB-PCXI on a synchrotron is the accessibility of large R_1 distances, which not only reduces the level of penumbral blurring [equation (1)] but also increases the spatial coherence of the beam through free space propagation (Paganin, 2006).

2.2.2. Measuring source size. The method of measuring source size employed for these experiments is detailed by Stevenson *et al.* (2010) and Gureyev *et al.* (2008). This method employs a dual-edge phantom, in this case two sheets of DuPont™ Kapton polyimide film crossed at 90° so as to measure the source size in both the horizontal and vertical directions simultaneously. At 30 keV, Kapton has minimal X-ray absorption [$\mu = 41.2 \text{ m}^{-1}$ (NIST, 2011)] and thus the images of the edges are dominated by phase contrast in the form of characteristic single black–white fringes. The contrast, C , and resolution, R , of these fringes were then measured, with C being defined as (Gureyev *et al.*, 2008; Stevenson *et al.*, 2010)

$$C = \frac{I_{\max} - I_{\min}}{I_{\max} + I_{\min}} \times 100\%, \quad (2)$$

where I represents the intensity values of the image. The observed resolution, R , is obtained from the spatial separation of the maximum and minimum intensity peaks, with reference to the object plane. The contrast and resolution values were then used to calculate the effective source size such that (Stevenson *et al.*, 2010)

$$C = \frac{R'\lambda|\varphi t|}{2\pi(2\pi e)^{1/2}\sigma_{\text{tot}}^2} \quad (3)$$

and

$$R = (4\sigma_{\text{tot}}^2 + R'\lambda)^{1/2}, \quad (4)$$

where $R' = R_2/M$ is the effective propagation distance corresponding to magnification M , λ is the wavelength, φ is the phase shift per unit length through the material, t is the thickness of the Kapton sheets and

$$\sigma_{\text{tot}} = [\sigma_b^2 + (M-1)^2\sigma_s^2/M^2 + \sigma_d^2/M^2]^{1/2}, \quad (5)$$

where σ_b , σ_s and σ_d are the standard deviations associated with the blurring of the edge, the source size and the detector point-spread function, respectively. The edge blurring, σ_b , was fixed at $4 \mu\text{m}$ in accordance with Gureyev *et al.* (2008) and Stevenson *et al.* (2010), and σ_d was measured to be $(18 \pm 2) \mu\text{m}$. The experimentally measured contrast and resolution of the Kapton phantom were then fitted to the expected theoretical values using a non-linear least-squares refinement to obtain the calculated source size. This method is described in more detail by Gureyev *et al.* (2008) and Stevenson *et al.*

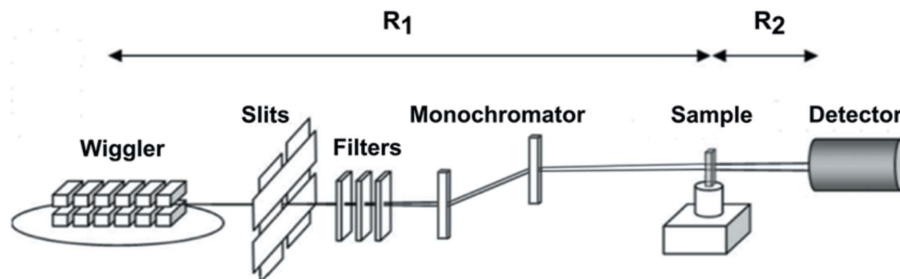


Figure 1

Experimental set-up for the PB-PCXI experiments performed on the IMBL. R_1 is the source-to-sample distance and R_2 is the sample-to-detector distance. Collimation of the beam in the horizontal direction was performed using the primary slits, shown in the figure. The effective source size in the vertical direction was varied by bending the crystals of the monochromator. Values for parameters used in both hutch 2B and 3B are given in Table 1 of the text.

(2010). Examples of alternative methods for measuring source size include Guigay *et al.* (2004) and Suzuki (2004), which was expanded by Morgan *et al.* (2010).

3. Experimental

3.1. Experimental set-up

Experiments were carried out on the IMBL of the Australian Synchrotron, with the synchrotron storage ring operating at 3 GeV and 200 mA. The RMS electron beam size in the straight sections is $320 \mu\text{m}$ horizontally and $16 \mu\text{m}$ vertically (Stevenson *et al.*, 2012), corresponding to Gaussian FWHMs of $754 \mu\text{m}$ and $38 \mu\text{m}$, respectively. The effective source size in the horizontal direction is dominated mainly by the size of the electron beam, as the electron-beam deviation caused by the field of the APS wiggler contributes little in comparison (Stevenson *et al.*, 2012). The X-ray beam supplied to the IMBL was produced by a 2.4 m-length Advanced Photon Source (APS) type-A permanent-magnet wiggler with $28 \times 8.5 \text{ cm}$ periods, operated at a gap of 15 mm, with a 1.4 T field.¹ A dual silicon Laue crystal monochromator was used to select the required energy of 30 keV. The angle of the crystal bend in the monochromator allowed the vertical effective source size to be altered, with the crystal bend (CB) being defined as

$$\text{CB} = \frac{\text{source-to-monochromator distance}}{\text{bending radius}}, \quad (6)$$

with the source-to-monochromator distance at the IMBL being 16.15 m. A positive CB indicates a concave bend of the crystals as seen by the source, thus increasing the effective source size in the vertical direction, and zero bending indicates flat unbent crystals. The bending of the monochromator crystals also allows the vertical size of the field of view at the sample position to be altered.

More information on the insertion device can be found by Stevenson *et al.* (2012). A diagram of the experimental set-up can be seen in Fig. 1.

¹ The APS wiggler has subsequently been upgraded to a superconducting multipole wiggler, newly installed but not yet optimized at the time of this writing (October 2013), as discussed further in §4.2.

In order to optimize image quality for PB-PCXI, three parameters were investigated: collimation of the beam in the horizontal direction *via* the primary slits, angle of curvature of the monochromator crystals (vertical direction) and sample-to-detector distance, R_2 (Table 1). Experiments were performed in two hutches of the IMBL: hutch 2B (31.7 m from the source) and hutch 3B (135 m from the source). Images were acquired by converting X-rays to visible light through a 25 μm terbium-doped gadolinium oxysulphide phosphor and Nikon 105 mm Macro lens set to maximum zoom (1 \times magnification) and then captured with a PCO.Edge CMOS detector with 2160 \times 2560 (height \times width) array. This provided an effective isotropic pixel size of 6.45 μm , giving a field of view of 13.9 mm \times 16.5 mm and an effective resolution of (42 \pm 4) μm FWHM of the point-spread function, which was determined *via* edge-spread function measurements. Exposure times ranging from 300 ms to 2 s were chosen, dependent on the effective source size and sample-to-detector distance, in order to fill the available detector dynamic range (16-bit A/D) for maximal signal-to-noise ratio without detector saturation. Images were pre-processed for flat-field (no sample) and dark-current image correction (no illumination) such that

$$\text{corrected image} = \frac{\text{image} - \text{dark}}{\text{flat} - \text{dark}}. \quad (7)$$

3.2. Image quality assessment

Evaluation of image quality was undertaken through imaging a series of perspex polymethyl methacrylate (PMMA) phantoms, including 1.5 mm-diameter spheres and 0.55 mm- and 1 mm-diameter vertically mounted cylinders. As a quantitative measure of image quality, the contrast and resolution of the cylinder edges were assessed as in §2.2.2. Image sets were assessed to determine the effect of varying the sample-to-detector distance and effective source size on images, in both the horizontal (collimation) and vertical (crystal bend) directions. This allows appropriate source parameters to be selected for a given flux requirement when performing live animal imaging in future work. Single-image transport-of-intensity phase retrieval, based on the algorithm by Paganin *et al.* (2002) which assumes a single isotropic non-magnetic material of known refractive index, was performed to determine whether the monochromaticity, coherence and detector set-up was sufficient to capture adequate fringe information for this retrieval to give accurate verification of the known sample volume. This method requires the input of the refractive and absorptive properties, δ and β , respectively, where the X-ray refractive index, n , of the material being analysed is given by $n = 1 - \delta + i\beta$. These values were obtained for PMMA at 30 keV from the National Institute of Standards and Technology (NIST) database (NIST, 2011), giving $\delta = 2.96 \times 10^{-7}$ and $\beta = 1.16 \times 10^{-10}$. The validity of using this algorithm at the R_2 distances used in this experiment is addressed by Paganin (2006, p. 325). For the phase retrieval to be viable

Table 2

Values of $(\lambda\pi R_2)^{1/2}$ at 30 keV for the sample-to-detector propagation distances used in hutch 3B.

If the feature size of the sample, a , is $\gg (\lambda\pi R_2)^{1/2}$ then the transport-of-intensity phase-retrieval algorithm is valid.

R_2 (m)	1.00	2.62	4.03	5.96
$(\lambda\pi R_2)^{1/2}$ (μm)	11.5	18.4	22.9	27.8

at sample-to-detector distance R_2 and wavelength λ , the Fresnel number, N_F , must be much greater than π , where

$$N_F \equiv \frac{a^2}{\lambda R_2}, \quad (8)$$

and a is the size of the smallest feature where the transport-of-intensity algorithm is still valid. Rearranging this formula to discern the smallest feature size that is still valid for the propagation distances used in this paper yields

$$a \gg (\lambda\pi R_2)^{1/2}. \quad (9)$$

Table 2 shows the values for $(\lambda\pi R_2)^{1/2}$ at 30 keV for the sample-to-detector propagation distances used in hutch 3B for this paper. The transport-of-intensity-based phase-retrieval method is valid as long as the smallest feature we are quantitatively analyzing is much greater than the stated value at each R_2 distance.

As can be seen, quantitative analysis of the 1 mm- and 3 mm-diameter cylinders *via* the transport-of-intensity-based phase-retrieval algorithm is valid at all R_2 distances used, as their diameters are much larger than the values displayed in Table 2, as per the validity requirements. Phase retrieval of the lung phantom CT images recorded at 1 m is also valid. Performing phase retrieval on the speckle images at the larger R_2 distances would be in the upper bounds of the validity region for this algorithm; however, such analysis was not performed in this paper. Additionally, the optimal distance for performing phase retrieval on a lung sample was investigated by Lovric *et al.* (2013) who state that the optimal distance for performing phase retrieval on lung samples is at p^2/λ , where p is the pixel size. As such, for pixels of 6.5 μm at 30 keV (4.133 $\times 10^{-11}$ m) the optimum R_2 is 1 m. This distance was used for CT of the lung phantoms, where phase retrieval of the glass spheres was applied during image processing.

3.3. Feasibility of propagation-based phase-contrast imaging of animal lungs on the IMBL

Lung image quality was evaluated by imaging lung phantoms comprised of large numbers of glass spheres (Kitchen *et al.*, 2004), ranging in diameter to emulate a range of typical mammalian alveoli sizes (Yagi *et al.*, 1999; Faffe *et al.*, 2002; Irvin & Bates, 2003). Three diameter ranges were used, 63–75, 90–106 and 106–125 μm . The spheres were suspended in either air for high-density speckle (approximate average packing fraction = 0.60) or agarose to simulate lung tissue

(approximate average packing fraction = 0.15). It is important to note that the density of these phantoms is inverted compared with a real lung (*i.e.* the glass ‘alveoli’ are of a higher density than the surrounding agarose or air ‘tissue’, whereas in a real lung the air-filled alveoli are of a lower density than the surrounding tissue). The change in δ as X-rays pass from air in the alveoli to surrounding lung tissue is approximately -2.65×10^{-7} (NIST, 2011), whereas $\Delta\delta$ for glass to the agarose in our samples is approximately 2.11×10^{-7} (NIST, 2011). While the reversed phase gradient will cause the intensity variations of the speckle pattern to be inverted, the characteristic size of the speckle pattern created is directly comparable with that of an actual lung of the same thickness, and the phase-contrast fringes will be affected in a similar manner due to the similar δ values. The phantoms used were 1 cm thick, which is approximately the same thickness in dorsal–ventral projection as a mouse lung. This makes the lung phantoms suitable samples for feasibility experiments, as variations to the speckle pattern from source size, sample-to-detector propagation distances *etc.* will be close to that of a real mouse lung (even though the intensity is inverted) and the speckle pattern can effectively be tracked for X-ray velocimetry.

Speckle pattern images obtained from the lung phantoms were assessed for image quality, with the mean intensity and standard deviation providing a means for comparing the speckle pattern under different conditions. From these images the contrast of the speckle pattern was calculated, with I_{\max} and I_{\min} taken as the intensity 2σ above and below the mean. Experimental images were compared with lung speckle simulations generated using the numerical simulation written by Ng *et al.* (2012) to validate the expected image quality, calculating the contrast as described above.

3.4. Feasibility of X-ray velocimetry on animal lungs at the IMBL

X-ray velocimetry is a technique used to study the flow of air through the lungs that is based on particle image velocimetry (PIV). PIV is a well established technique commonly used in fluid mechanics to measure the flow and movement of particle-laden fluids (Adrian, 2005; Fouras *et al.*, 2012). Conventionally used to image optically transparent systems with lasers, PIV has been extended in recent years to optically opaque systems, such as biological objects, with the use of X-rays (Fouras *et al.*, 2009a,b). The advancement of ultra-fast detector systems and the development of phase-contrast imaging has increased the applicability of this technique to live imaging *in vivo*, namely to the speckle patterns created from the blood (Irvine *et al.*, 2008; Jamison *et al.*, 2011) and the lungs (Dubsky *et al.*, 2012a; Fouras *et al.*, 2012). This has led the application of PIV to biological systems without particles to be dubbed X-ray velocimetry (XV). In PIV and XV, movement or flow of the sample is determined by statistically analysing two images separated by a known time interval. The image pairs are divided into many sampling windows known as interrogation windows, and analysed by

cross-correlation to produce correlation peaks, of which the location of the maximum peak shows the inter-frame displacement for that interrogation window. This displacement can then be displayed as a velocity vector given the known time-lapse between image frames. In propagation-based phase-contrast XV of the lungs, the speckle pattern created from the lungs provides the pattern through which the movement can be traced. Post-processing can then allow the user to map local lung expansion (Dubsky *et al.*, 2012a; Fouras *et al.*, 2012) and air flow through the lungs (Dubsky *et al.*, 2012a).

In this experiment, ten images were recorded of each sample (glass beads in air or agarose gel) on the beamline. The images did not undergo flat-dark correction, as this commonly used pre-processing step does not necessarily improve the accuracy of XV, but usually decreases the signal-to-noise ratio of the image. Image pairs were then created for XV analysis. The initial time point, T_0 , was the first image (image 1) taken of the sample. To simulate the lung moving, the last image of the sample (image 10) was rotated 5° clockwise (in the xy plane), and this image became the next time point, T_1 . Each image pair was then cropped to 300×300 pixels to eliminate errors caused by missing corner information at the edges by missing particles due to rotation of the images. The pair was then discretized into interrogation windows of 16×16 pixels, with a 50% overlap, and cross-correlation performed. An iterative approach was used, whereby the first iteration provides an estimate of the displacement. Subsequent iterations are performed with the second image region being offset by this estimate, producing a detailed quantitative vector field whilst reducing errors associated with parts of tissue leaving the interrogation region. The universal outlier detection method was employed to eliminate errors due to false measurements (Westerweel & Scarano, 2005). X-ray velocimetry error analysis was undertaken by creating an exact vector map for the rotation of the image pair, and subsequently subtracting this theoretical vector map from the experimental vector map. For more information on the processes described here, the reader is referred to Fouras *et al.* (2007, 2009a,b, 2012), Dubsky *et al.* (2010, 2012b) and references therein.

3.5. CT of lung phantom samples

Tomographic data sets were obtained of each of the lung phantoms in hutch 3B at 30 keV for characterization of the sample and sphere diameters. 1500 projections were collected over a 180° rotation in 0.12° steps. Images were collected using a 2 s exposure at a propagation distance of 1 m. In addition to flat- and dark-field correction, single-image phase retrieval, as mentioned above, was also carried out for the data set, with $\delta/\beta = 5.91$ for the glass–agarose interface and $\delta/\beta = 81.57$ for glass–air at 30 keV. CT reconstruction was performed using Shepp–Logan filtered back-projection assuming a parallel beam. Data processing and analysis was performed using *X-TRACT* (version 4) <http://ts-imaging.net/Services/> (Gureyev *et al.*, 2011).

Table 3

Summary of the increasing trend in contrast values associated with propagation distances taken from the 30 keV, CB = 0, 15 mm PSW data set.

R_2 (m)	Contrast (%)	
	Horizontal direction	Vertical direction
0.25	1.18 (0.02)	1.05 (0.02)
1.48	2.46 (0.03)	3.35 (0.05)
4.03	3.71 (0.05)	8.6 (0.1)
5.96	4.50 (0.04)	11.4 (0.3)

Table 4

Speckle pattern visibility of lung phantoms of high-density solid glass spheres of various diameters suspended in air, at various sample-to-detector distances.

Diameter of solid glass spheres in air	Speckle pattern definable at R_2 ?			
	1.00 m	2.62 m	4.03 m	5.96 m
106–125 μm	Yes	Yes	Yes	No
90–106 μm	Yes	Yes	No	No
63–75 μm	Yes	No	No	No

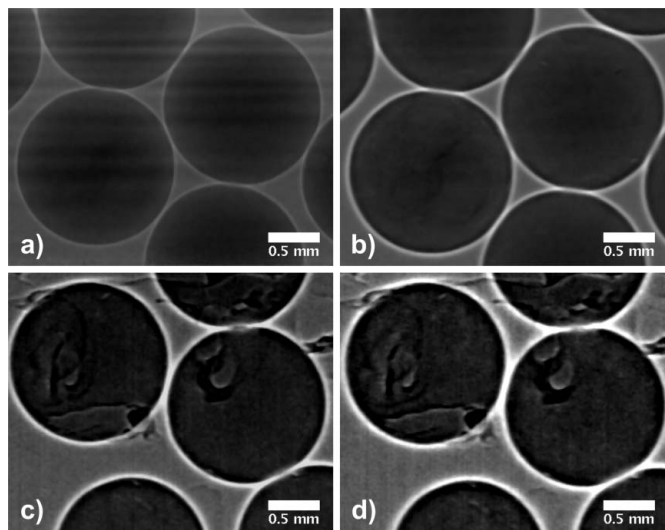


Figure 2

Perspex spheres of 1.5 mm diameter enclosed in Kapton tape imaged at 30 keV, crystal bend = 0, at 15 mm PSW taken at (a) $R_2 = 0.25$ m and (b) $R_2 = 1.48$ m in hutch 2B and (c) $R_2 = 4.03$ m and (d) $R_2 = 5.96$ m in hutch 3B. The grey scale of the images has been normalized for display purposes, and are quantitatively comparable between sub-images.

4. Results and discussion

4.1. Effect of sample-to-detector propagation distance on image quality

As expected, an increase in propagation distance R_2 improved the visibility of the images of the standard PMMA sphere and cylinder phantoms, with greater detail becoming visible as the distance was increased from 0.25 m to 5.96 m. Fig. 2 shows an increase in the visibility of the Kapton tape holding the spheres in place, with the rough edge of the tape and the air bubbles seen most prominently in the $R_2 = 5.96$ m image (Fig. 2d). Edge (phase) contrast also increased substantially, as can be seen in Table 3, which reports the contrast measured in both the vertical and horizontal directions from the dual-edge Kapton phantom, imaged at 30 keV, CB = 0, with 15 mm primary slit width (PSW) in the horizontal direction.

The benefits of being able to extend R_2 to such large distances in hutch 3B of

the IMBL becomes particularly apparent when comparing images of the lung phantoms consisting of 90–106 μm -diameter solid glass spheres suspended in agarose, such as those seen in Fig. 3. The speckle pattern produced by the spheres can be seen in the high-density areas of the sample at $R_2 = 1$ m; however, individually suspended spheres are only more clearly defined when the propagation distance is increased, such as can be seen in Fig. 3(c) at $R_2 = 5.96$ m. The edge enhancement provided by the large R_2 distances is promising for imaging small structures of the lung and airways.

Whilst high-contrast speckle patterns were produced for the agarose-based lung phantoms at all R_2 distances listed in Table 1, this was not the case for the high-density lung phantoms of solid glass spheres in air with visibility of the speckle pattern varying between R_2 distances dependent on sphere size, as can be seen in Table 4.

The decrease in speckle visibility with smaller sphere diameters at high sample packing fractions ($\sim 60\%$) is due to a combination of (i) penumbral blurring from the large horizontal effective source size, (ii) the fringe width of the spheres at large R_2 distances overlapping such that the sphere edge becomes undefinable at high packing densities, and (iii) the effect of the photons scattering in the air path between the sample and detector, as discussed in §4.3. The combination of these factors reduces the resolution of the system, such that the speckle pattern produced by the spheres is blurred to the extent at which it is no longer distinguishable. This is analogous to a wavefront from an incoherent source that has large phase variations, which smooth out and become more coherent the further from the source it propagates. Small animal lung composition has a refractive index decrement that

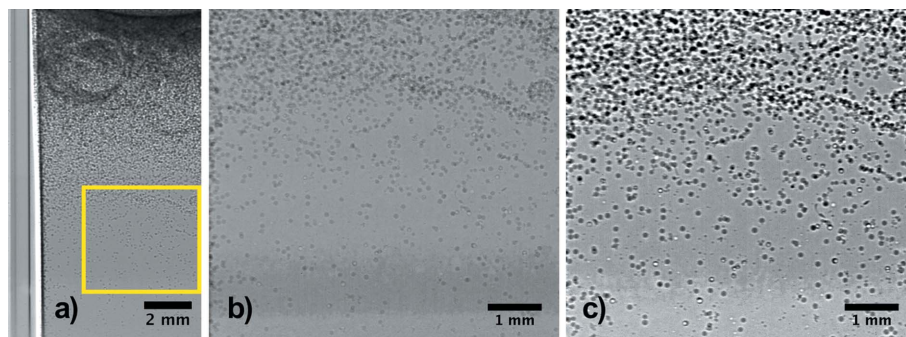


Figure 3

(a) Lung phantom sample of solid glass spheres of 90–106 μm diameter suspended in agarose gel, imaged at 30 keV, CB = 0, 15 mm PSW, $R_2 = 1$ m, with the inset showing an area of individually suspended spheres at (b) $R_2 = 1$ m and (c) 5.96 m. The grey scale is the same for all three images.

Table 5

Average contrast of the speckle pattern obtained from lung phantom of 63–75 μm -diameter solid glass spheres in air, at the maximum and minimum effective source size settings, 30 keV, hutch 2B, $R_2 = 1$ m with a 0.5% uncertainty.

	Lung phantom speckle average contrast (%)	
	2 mm	15 mm
CB = 0	25.1	23.3
CB = 1.5	23.8	24.1

is closer in magnitude to that of the agarose-based lung phantoms than the air-based phantoms, yet has an alveoli packing density between the agarose and air-based phantoms. With this in mind, experiments imaging whole mouse lungs might utilize an R_2 distance of between 1 and 4 m, and experiments concerning areas of the lungs where alveoli density is reduced might better employ an R_2 distance of greater than 2.5 m based on these phantom studies. These distance ranges are supported by similar studies in real lungs by Kitchen *et al.* (2004, 2008) and Lewis *et al.* (2005). Our study demonstrates that experiments imaging the airways could employ an R_2 distance of up to 4 m and beyond on the IMBL. These distances should be reviewed for increases in lung thickness, such as in rabbits and larger animals, and for the differing energies likely to be employed for higher penetration.

4.2. Effect of source size variations on image quality

Analysis of images recorded under various effective source size conditions in both the horizontal (varied by altering collimation) and vertical (varied by crystal bending) directions was undertaken through quantitative analysis of contrast observed from the Kapton edge phantom.

4.2.1. Hutch 2B. In hutch 2B the effective source size made a noticeable difference to the illuminated field of view. Collimation of the beam to 15 or 5 mm PSW in the horizontal direction allowed the full X-ray field of view to be observed, but collimation to 2 mm PSW reduced the field of view with uniform illumination by $(60 \pm 3)\%$. However, analysis of the Kapton phantom again showed little difference in image quality within the centre of the image. Speckle analysis from the lung phantoms showed very little variation in contrast with differing source size, as shown in Table 5.

It is important to mention here that the exposure time for images captured in hutch 2B with CB = 0 was 1 s, whilst the exposure time for images taken with CB = 1.5 was 300 ms to acquire the same number of counts. From this, lung imaging in hutch 2B is advised to be undertaken at 15 mm PSW with a crystal bend in the region of 1.5. Whilst this combination does not necessarily provide the highest contrast image, the benefits of not limiting the field of view and short exposure times outweigh the minimal decrease in contrast.

4.2.2. Hutch 3B. Results from hutch 3B showed that variations in the effective source size made no significant impact on image contrast as can be seen in Fig. 4. Analysis of the Kapton dual-edge phantom showed a minor general trend

Table 6

Contrast values observed for the Kapton dual-edge phantom at the maximum and minimum effective source size settings.

Values for both the horizontal smoothing effect to the image (vertical Kapton edge) and the vertical smoothing effect (horizontal Kapton edge) are shown for the 30 keV, hutch 3B, $R_2 = 5.96$ m data set, with an estimated uncertainty of $\pm 0.3\%$ for the Kapton phantom.

	2 mm primary slit width	15 mm primary slit width
Kapton, horizontal contrast (%)		
CB = 0	4.8	4.5
CB = 2	5.0	4.4
Kapton, vertical contrast (%)		
CB = 0	11.8	11.4
CB = 2	11.6	11.1

of decreasing contrast with increasing effective source size, an example of which is shown in Table 6, but this did not result in any observable qualitative difference.

The results in Table 6 do not show a significant impact on image quality with variations in effective source size by collimation or crystal bend. It is suggested that any of the effective source sizes produced from 2–15 mm primary slit width and $0 < \text{CB} < 2$ can be utilized for PB-PCXI experiments

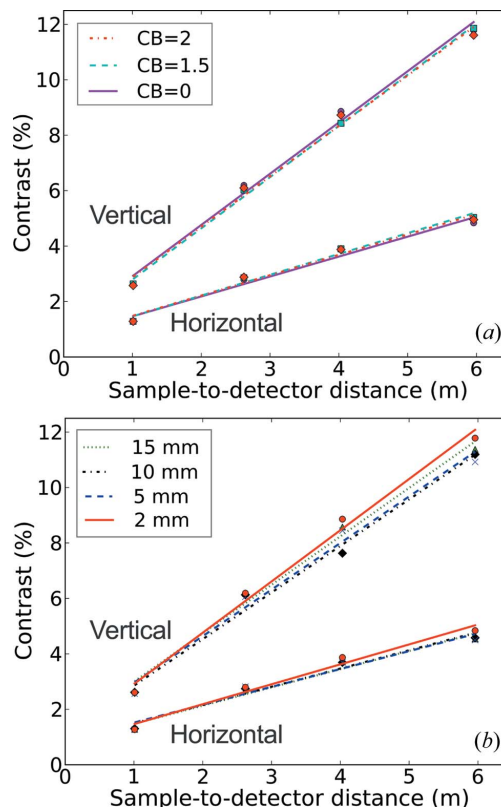


Figure 4

Measured contrast in both the horizontal and vertical directions with variations in effective source size. Whilst contrast increases with R_2 , and is higher in the vertical direction than the horizontal, no significant difference is seen between changes in (a) vertical effective source size through crystal bending or (b) the horizontal effective source size through beam collimation.

Table 7

Measured effective source size, Gaussian FWHM, calculated from Kapton edge data taken in hutch 2B.

Crystal bend	Effective horizontal source size, FWHM (μm)			Effective vertical source size, FWHM (μm)
	2 mm PSW	5 mm PSW	15 mm PSW	
0	660 (190)	660 (190)	800 (180)	25 (fixed)
1.5	610 (160)	970 (160)	990 (110)	510 (200)

of lungs in hutch 3B. Imaging of the lungs in small animals, such as mice and rabbits, may benefit from the slightly higher contrast observed through a 2 mm PSW and $\text{CB} = 0$, as the small effective source size employed will reduce the penumbral blurring of small structures of the lungs. Additionally, the reduction in X-ray flux will reduce the radiation dose to the animal without comprising image quality. However, the 2 s exposure time utilized is too long to image live animals during respiration, given a respiratory period of 0.5 s or less in small animals (Blackstone *et al.*, 2005; Carnibella *et al.*, 2013). A reduction in exposure time to < 50 ms, as is required to image lung motion without significant motion blur (Kitchen *et al.*, 2008; Dubsky *et al.*, 2012a; Fouras *et al.*, 2012), would result in less than 100 counts per pixel through 1 cm of agarose in a single image, which is insufficient to resolve anatomic information or perform XV analysis.

However, such imaging is likely to be achievable with the new superconducting multipole wiggler (SCMPW), as seen in §4.7. The SCMPW has recently been installed at the time of writing (October 2013) and consists of 30 periods in total, with a period length of 5.2 cm, with capabilities to reach 4.2 T, though it is not yet operating at full field strength. Additionally, the pixel size of $6.5 \mu\text{m}$ utilized for this study is significantly smaller than is commonly used in live animal lung imaging (as described in §2), thus an increase in pixel size will allow for more photons to be captured during a single exposure, reducing the required exposure time to reach the same number of counts as seen in these studies with the same experimental set-up.

4.3. Source size calculations

The effective source size was calculated as described in §2.2.2 from data recorded in hutch 2B, with the results shown in Table 7.

As is expected with the wiggler source, it can be seen that the horizontal effective source size at the IMBL is large (of the order of 800–1000 μm in diameter). Also as expected, it can be seen that bending the monochromator crystals substantially increases the effective source size in the vertical direction. A significant increase in effective source size occurs between PSWs of 2 and 15 mm of the beam both with and without crystal bending. It is

noteworthy that this increase occurs for different collimations of the beam dependent upon the amount of crystal bending. This indicates that variations in crystal bend, which were thought to only affect the vertical effective source size, may also influence the horizontal effective source size. This is supported by the images taken at 5 mm PSW, an example of which is shown in Fig. 5. These images show that, even at the same collimation, different crystal bending results in different illumination at the edge of the image (the sample has not moved between images). The increased source size with $\text{CB} = 1.5$ increases the illumination field size in the horizontal direction such that the edge of the illuminated field is no longer obvious, unlike the $\text{CB} = 0$ image. This could be due to mechanical properties associated with bending the crystals in the monochromator, or other beamline characteristics, such as the heat load on the first crystal of the monochromator. In any case, our results indicate that there is not a simple relationship between collimation and observed source size on this beamline.

When this crystal bending effect is coupled with the intensity distribution of the beam, it can be seen how a significant difference in effective source size can occur over small changes in collimating distance. It seems that the majority of the beam intensity is concentrated around the central axis of the beam. Without crystal bending, the source size was approximately static up to 15 mm PSW, but with crystal

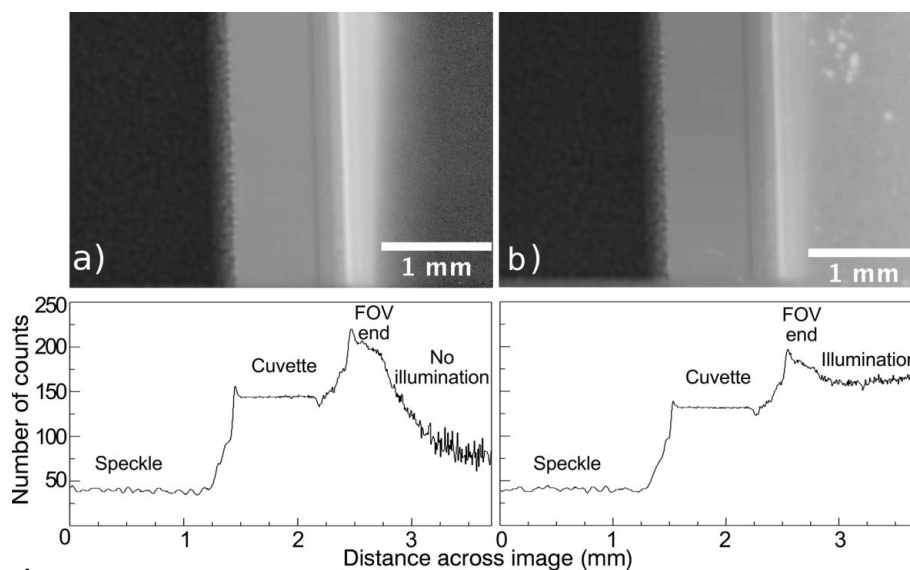


Figure 5 Image of a lung phantom of 63–75 μm -diameter solid glass spheres in air imaged at 30 keV, $R_2 = 1$ m, 5 mm PSW, hutch 2B, with (a) $\text{CB} = 0$ and (b) $\text{CB} = 1.5$. It can be seen that illumination in the horizontal direction is increased with an increase in CB, indicating that varying the CB affects not only the vertical effective source size but also the horizontal.

Table 8

Predicted and observed values for horizontal and vertical contrast taken from hutch 3B, 30 keV, crystal bend = 0, 15 mm PSW Kapton edge data. It can be seen that the observed value is much less than the predicted value in the horizontal direction.

R_2 (m)	Horizontal contrast (%)			Vertical contrast (%)		
	Predicted	Observed	% of predicted	Predicted	Observed	% of predicted
2.62	7.00	2.69	38.4	6.96	6.18	88.8
4.03	8.80	3.71	42.2	10.08	8.58	85.1
5.96	9.84	4.54	46.1	13.40	11.38	84.9

bending a PSW of as little as 5 mm caused an increase in effective source size due to the divergence of light in the horizontal direction. This effect can have multiple influences on experiments performed on the IMBL, particularly for experiments performed in hutches closer to the source. Users should note that increasing the vertical effective source size by bending the crystals, for instance to increase the vertical beam size or field of view, will also result in an increase in the horizontal effective source size. A favourable consequence of this may be that greater effective horizontal source sizes, and thus beam sizes, are achievable with bending of the monochromator crystals when the beam is at maximum width (*i.e.* no beam collimation). Unfavourable consequences might include reduced phase contrast from decreased source coherence and slight blurring of the image in the horizontal direction, due to penumbral blurring, caused by the increased effective horizontal source size.

A source size determination was also attempted from the data recorded in hutch 3B; however, the observed contrast and resolution values were not as expected from the effective source dimensions found from the 2B data. In the horizontal direction the observed contrast was only $(41 \pm 4)\%$ of the predicted contrast, calculated using the least-squares refinement and equation (3) as discussed in §2.2.2, and the resolution was $(170 \pm 20)\%$ of the predicted value [equation (4), §2.2.2]. Values in the vertical direction for the contrast were $(86 \pm 7)\%$ of the predicted values, and the the resolution was $(90 \pm 10)\%$ of the predicted values. An example of this is given in Table 8 for the CB = 0, 15 mm PSW data set.

Whilst the results presented in §4.2 suggest that the changes to image quality as a function of effective source size may not be sufficient to accurately determine the effective source size, the extent of the discrepancies between the expected and observed contrast and resolution values, particularly in the horizontal direction, are non-negligible. Whilst the geometry of the source, and by association the divergence of the beam, will increase the blurring in the horizontal direction, this is accounted for in the predicted values through the σ_s term [equation (5)]. The equations and code used to calculate these predicted values have been validated previously by Stevenson *et al.* (2010) and microfocus laboratory X-ray source experiments. One potential factor for the discrepancies between the predicted and observed values is the large R_2 distances employed in hutch 3B, which provide sufficiently large distances for significant air scattering to occur. As can be seen in Fig. 6, photons propagating through 6 m of air will have a 23% reduction in intensity compared with those exiting the

sample, or passing through vacuum. This scattering is made up of coherent and incoherent scattering, as well as photoelectric absorption.

Whilst an R_2 distance of 1 m was utilized in both hutches, the results did not appear to be affected by scattering to the same extent. Contrast in hutch 3B was reduced by 2.8% for the vertical direction (horizontal Kapton edge) and

41.7% for the horizontal direction (vertical Kapton edge), when compared with hutch 2B. The higher contrast observed in hutch 2B may be due to the smaller propagation distance between the end of the vacuum pipe and the sample in hutch 2B, which was approximately 20 cm, compared with approximately 1.5 m in hutch 3B. This extra distance in hutch 3B that the photons travel in air before they pass through the sample will slightly increase the amount of scattering observed, such that images taken at $R_2 = 1$ m in hutch 3B will be affected more strongly than images taken at $R_2 = 1$ m in hutch 2B, thus reducing the image contrast. Additionally, synchrotron radiation is plane polarized, which theoretically leads to preferential scattering in the horizontal direction and will hence degrade the resolution more in the horizontal plane (*i.e.* the contrast measured across the vertical Kapton edge), compared with in the vertical plane. The effects of polarization on scattering were investigated through the simple case of polarized light colliding inelastically with a free electron at rest. Depaola (2003) notes that, while non-polarized light will scatter uniformly, inelastic scattering of polarized light from a free electron at rest at angle θ will have a dependence on angle φ , relative to the polarization, such that (Depaola, 2003)

$$d\sigma = \frac{1}{2} r_0^2 d\Omega \frac{k^2}{k_0^2} \left[\frac{k_0}{k} + \frac{k}{k_0} - 2 \sin^2 \theta \cos^2 \varphi \right], \quad (10)$$

where σ is the differential cross section for an inelastic collision where the photon is scattered at a particular angle θ in the

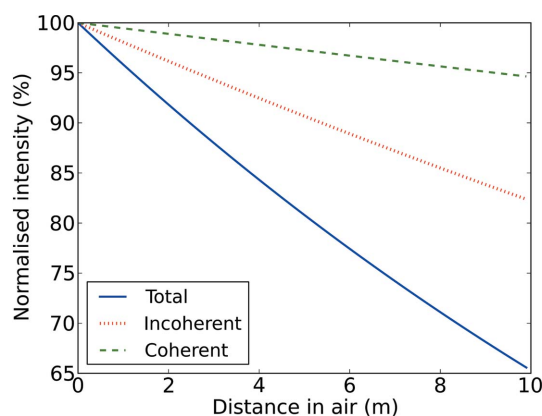


Figure 6 Transmission of photons in air at 30 keV as a function of distance. Both coherent (green dashes) and incoherent (red dots) scattering contribute to the total scattering (blue solid) seen, which affects the total transmission of photons. Scattering cross sections for air at 30 keV were obtained from the NIST database (NIST, 2011).

vertical plane and φ in the horizontal plane, k_0 is the incident energy of the photon, k is the energy of the scattered photon, Ω is an infinitesimal solid angle and r_0 is the classical electron radius. The differential cross section for a 30 keV polarized photon undergoing Compton scattering with a free electron at rest was plotted over $0 < \theta < 180^\circ$ and $0 < \varphi < 180^\circ$, which can be seen in Fig. 7.

This result shows that polarization of the incident light does indeed have an effect on φ in the range $20 < \theta < 160^\circ$. However, for the photons scattered from the sample to still hit the $1.4 \times 1.65 \text{ cm}^2$ detector (where the beam is aligned with the centre of the detector) at $R_2 = 1 \text{ m}$, they must be scattered at $\theta \leq 0.40^\circ$ and $\varphi \leq 0.47^\circ$ (assuming a single scattering event). Within this region, it can be seen that the scattering of photons

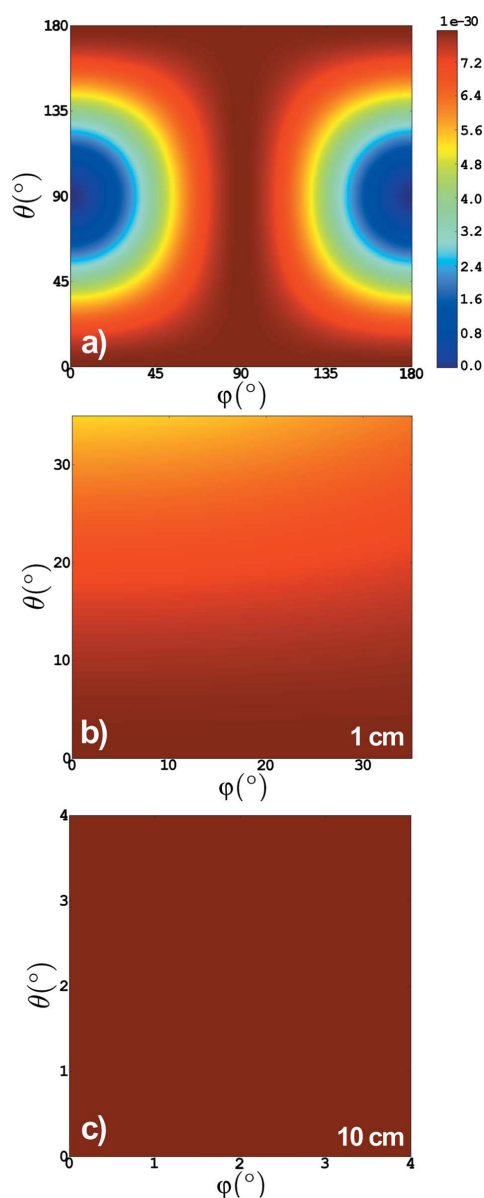


Figure 7 (a) Differential cross section of a horizontally polarized photon scattering inelastically from a free electron at rest as a function of horizontal scattering angle φ and vertical scattering angle θ from 0 to 180° , (b) for a single event 1 cm from the detector and (c) for a single event 10 cm from the detector.

is largely uniform. However, if the distance from the scattering point to the detector is decreased such that photons undergo a scattering event within 1 cm of the detector, the acceptance angle for scattered photons to hit the detector is increased to $\theta \leq 35^\circ$ and $\varphi \leq 40^\circ$. Within 1 cm from the detector, polarization does have an effect on the scattering of the photon, as can be seen in Fig. 7(b). Yet, this polarization effect is minimal at 7 cm and effectively non-existent by 10 cm, as seen in Fig. 7(c). To explore the contribution that these polarized photons scattering close to the detector ($< 10 \text{ cm}$) would have to the overall blurring of the image in each direction, the amount of horizontal and vertical scattering from horizontally polarized photons moving through 0–6 m of air was plotted (Fig. 8).

It can be seen from the maximum gradient of cumulative scatter between 0 and 2 m that photons scattering close to the detector ($< 2 \text{ m}$) contribute more to the blurring of the image (Fig. 8). It can also be seen that there is negligible difference between the effect of horizontal and vertical scattering on the overall image. Whilst photons scattering directly in front of the detector may be influenced by polarization, the majority of photons will not be affected, especially at R_2 distances of up to 5.96 m. Thus, it can be concluded that while polarization of the incident photon beam may contribute to preferential blurring in the horizontal plane in the hutch 3B data, it is not the major contributing factor. Having explored all reasonable aspects of the beamline and experimental set-up, the cause for this additional preferential blurring in the horizontal plane of the images taken in hutch 3B is still unknown and requires further investigation; however, such investigation is beyond the scope of the current paper.

In summary, the collective results seen here in §4.3 indicate that for experiments imaging small detail structures, such as the lungs and airways of small animals, in hutch 3B of the IMBL, it would be beneficial to introduce a medium between the sample and detector which reduces the scattering of photons, such as a helium-filled or vacuum tube. This will improve the resolution of the images, allowing small features (approaching the micrometre level) to be more accurately resolved. Preferential blurring was observed in the horizontal plane, the cause of which is still open to investigation.

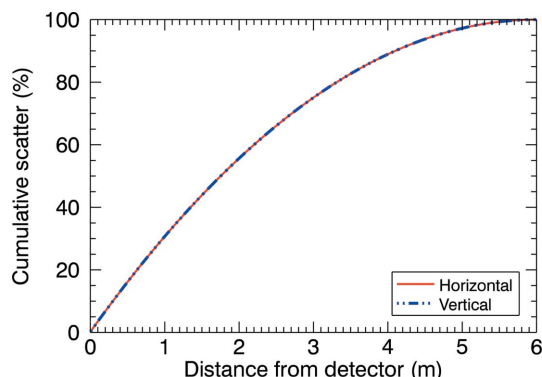


Figure 8 The cumulative scatter obtained in the horizontal and vertical directions from horizontally polarized photons over 6 m in air. It can be seen that there is no difference between the horizontal and vertical directions.

4.4. Phase retrieval

Single-image phase retrieval (§3.2) was performed on the cylinder samples to ascertain whether quantitative reconstruction of the projected thickness of the object was possible for images obtained on the IMBL. The reconstructed diameters of the cylinders were consistent throughout the 0.25–4.03 m data sets, with the average diameter of the 1 mm cylinder measured at (1.0 ± 0.1) mm and the 0.55 mm cylinder at (0.55 ± 0.03) mm. Overall, most of the images were reconstructed as an accurate representation of the shape and thickness of the cylinders, such as can be seen in Fig. 9. However, some images contained intensity fluctuations in the flat field, caused by vertical displacement, or ‘wobbling’, of the beam between frames. These variations caused a thickness to be recorded in the background of the image where there was no object, and thus over-estimated the thickness of the cylinder near the intensity variations. The diameters of the 5.96 m data set were less precise, with measured diameters of (1.0 ± 0.6) mm and (0.6 ± 0.1) mm, respectively, with most of the error arising at the edges of the object where the phase gradient is infinite. This suggests that an R_2 distance of approximately 4 m is the upper limit for accurate single-image phase reconstruction on IMBL using this algorithm and for

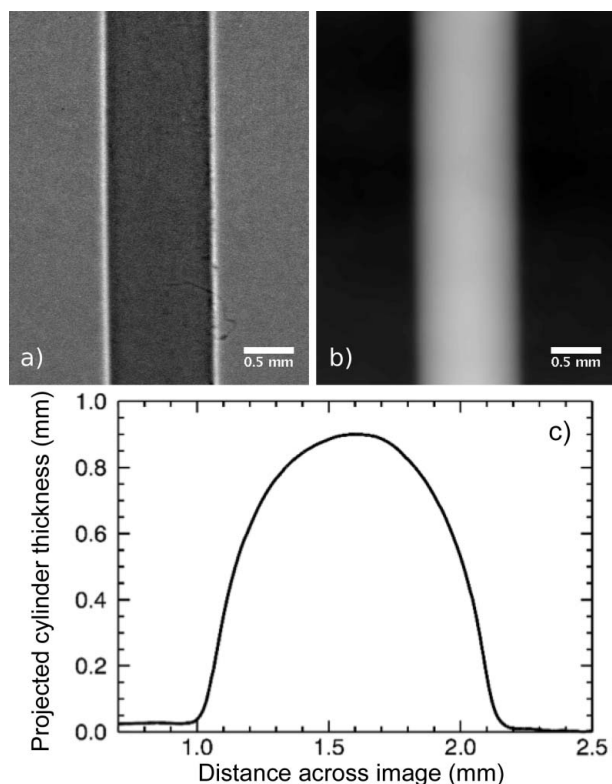


Figure 9 PMMA cylinder of 1 mm diameter (a) imaged at 30 keV, CB = 0, 2 mm PSW with $R_2 = 4.03$ m. (b) Phase-retrieved image (Paganin *et al.*, 2002) with $d = 2.96 \times 10^{-7}$ and $b = 1.16 \times 10^{-10}$, where the grey scale is proportional to the thickness of the object. Analysis of the phase-retrieved image shows an accurate measurement of the known diameter of the cylinder, as can be seen in (c) the average line profile of (b), showing the width and depth of the cylinder to within 10% of the known value.

this sample. This could be attributed to the level of scattering of photons through air at this distance, as discussed in §4.3.

4.5. Lung speckle X-ray velocimetry analysis

XV analysis of the experimental speckle images was successful across the data set for both the glass–air and glass–agarose lung phantoms at all R_2 distances. Of particular interest, XV analysis of the smallest-diameter high-density lung phantom speckle, which encountered a high degree of blurring at increasing R_2 as discussed in §4.1, produced a good XV vector map at not only $R_2 = 1$ m but also at 5.96 m, as can be seen in Fig. 10.

XV vector maps that exhibit a RMS vector error of less than 1 pixel are deemed to be acceptable (Dubsky *et al.*, 2012b). An

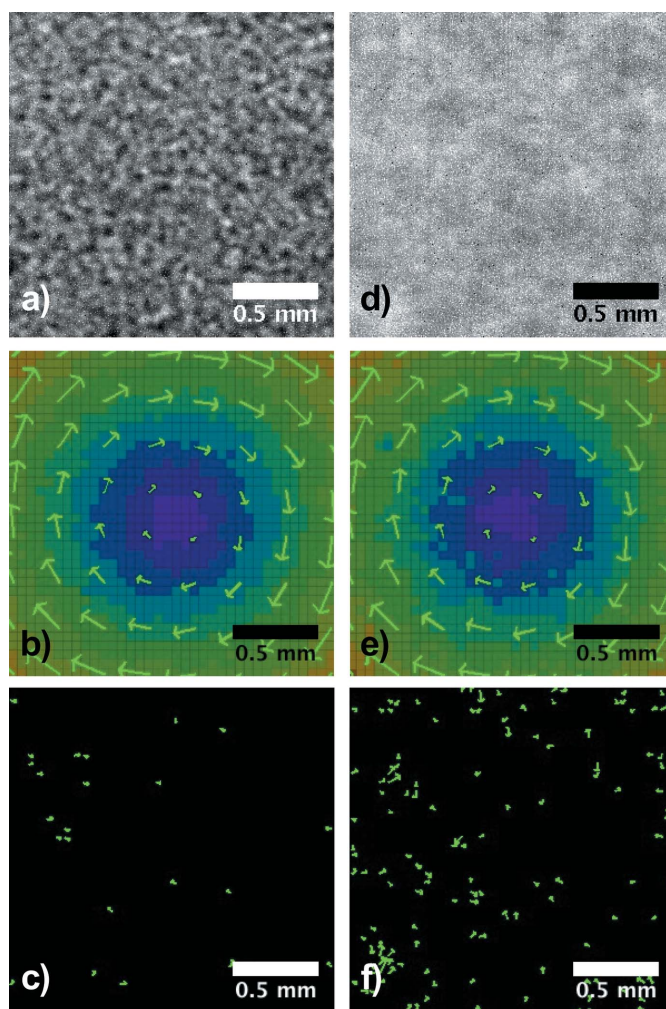


Figure 10 (a) Speckle pattern produced from 63–75 μ m glass spheres in air, imaged in hutch 3B at 30 keV, CB = 0, 15 mm PSW, $R_2 = 1$ m. (b) X-ray velocimetry vector map obtained through analysis of a 5° clockwise rotation between the image pair from (a), as described in §3.4. The contour map shows the relative magnitude of the motion vectors seen, with the largest shift seen at the edges of the image. Only one in five vectors are displayed in this image for ease of viewing. (c) Vector map of the X-ray velocimetry errors. All of the vectors are shown, and the magnitude is to the same scale as that shown in (b). (d)–(f) show the same images as (a)–(c); however, $R_2 = 5.96$ m.

Table 9

Error vector results from X-ray velocimetry analysis of the speckle produced from 63–75 μm glass spheres in air, imaged in hutch 3B at 30 keV, CB = 0, 15 mm PSW.

The error vectors were calculated by subtracting the experimental X-ray velocimetry vectors from a theoretical exact vector field. The vector average, which should be at the centre of rotation (0 pixels), the root-mean-squared (RMS) error, and percentage of rejected vectors are shown for both the x and y directions.

R_2 (m)	Vector component	Average (pixels)	RMS error (pixels)	Rejected vectors (%)
1.00	x	0.05	0.50	0.2
	y	0.02	0.44	
2.62	x	−0.04	0.59	0.8
	y	0.01	0.59	
4.03	x	0.02	0.64	1.2
	y	0.00	0.62	
5.96	x	0.03	0.64	4.0
	y	−0.03	0.65	

additional measure of accuracy is the number of experimental vectors rejected by the algorithm. Less than 1% of vectors rejected is considered to be an accurate vector map, while 3–4% is deemed borderline acceptable. From Table 9 it can be seen that each image pair has a RMS error of less than 1 pixel in the x and y vector directions, showing that both XV data sets have an acceptable level of error for the experimental vectors recorded. The $R_2 = 1$ m data set has a lower RMS error, as expected due to the clearer speckle pattern. The small number of rejected vectors for $R_2 = 1$ m also supports the accuracy of this result. The increase in rejected vectors for the $R_2 = 5.96$ m image set, compared with the $R_2 = 1$ m image set, was expected due to the reduced contrast and larger characteristic length scale of the speckle pattern due to blurring; however, the relative percentage of rejected vectors is still at a borderline acceptable level.

These results show that XV can successfully be carried out on a lung phantom image of relatively poor quality, measured by contrast and feature size as required for XV, where in this case the blurring of the sample image has reduced the contrast and blurred the speckle pattern. These results particularly highlight the ability for X-ray velocimetry to be performed on lung images without a high-contrast speckle pattern being visible to the human eye. It is noted by Ng *et al.* (2012) that (i) an optimal phase-contrast image of lung speckle (high visibility) does not necessarily provide optimal XV cross-correlation, (ii) that an increase in noise does not necessarily degrade the accuracy of XV, and (iii) that some blurring of the image, often caused by penumbral blurring, can improve the accuracy of the XV analysis. This is achieved by smoothing the noise peaks, thus enhancing the signal-to-noise ratio and allowing the correlation peak that determines the XV vector to be more accurately located.² However, the results of Ng *et al.*

² It is important to note here that too much image blurring diminishes the defining features of the speckle pattern, which degrades the XV analysis. Consequently, a trade-off occurs for XV between using a source that is sufficiently large to provide enough intensity for fast imaging, whilst also being sufficiently small to have an acceptable degree of penumbral blurring to maintain the accuracy of the velocimetry (Ng *et al.*, 2012).

(2012) were simulated to a maximum R_2 of only 4 m and did not take into account other experimental factors such as blurring due to scatter. The experimental results presented here, of R_2 up to 5.96 m, extend the perceived limitations of phase-contrast X-ray velocimetry of the lungs. Such a result is promising for the successful application of this method to live animals such as mice, and possibly larger animals such as sheep, on the IMBL in the future.

4.6. Computed tomography

CT data were obtained of the 90–106 μm low sphere-density phantom of solid glass spheres suspended in agarose and high sphere-density sample of solid glass spheres in air, in order to assess the three-dimensional imaging capabilities of the IMBL and to characterize the lung phantoms. From the manufacturer’s description, this sphere range has a mean diameter of 98 μm with a standard deviation of 24 μm (Whitehouse Scientific Ltd). Fig. 11 shows cross sections of phase-retrieved data sets of both samples.

The cross sections of the spheres from the high-density sample (Fig. 11*b*) were difficult to determine, indicating that the high packing density caused multiple refractions of the spheres to occur, and thus the packing fraction of this sample is too high for single-image phase retrieval to successfully reconstruct the individual spheres. Additionally, it may be that too much phase contrast was observed. This did not appear to affect the low packing density sample; however, too much phase contrast (*i.e.* wide and/or multiple fringes) would become problematic at high packing fractions as fringes from neighbouring spheres overlap and the sphere boundaries become less defined. The individual spheres in the agarose sample, however, were identifiable and cross-sectional areas were measured using *Fiji* (<http://fiji.sc/Fiji>). The measured diameters were $\mu = 75$ μm and $\sigma = 32$ μm , compared with the manufacturer’s $\mu = 98$ μm and $\sigma = 24$ μm . The measured values are likely an underestimation, as a single CT slice will not intersect the middle of every sphere, but will more likely intersect towards the top or bottom of some spheres. This can be accounted for by applying a calibration factor, which integrates over the height of the sphere to sum all radii in the horizontal plane of the sphere, such that the calculated maximum cross section of the sphere, d_{max} , is equal to

$$d_{\text{max}} = (4/\pi) d_{\text{m}}, \tag{11}$$

where d_{m} is the measured cross section of the spheres from the CT image. With this calibration, the measured cross section of the spheres is now $\mu = 95$ μm and $\sigma = 41$ μm , showing better agreement with the manufacturer.

A three-dimensional rendering of one of the glass spheres in agarose samples was also undertaken. This sample was chosen due to the distribution of spheres through the sample, with a higher density of spheres at the bottom of the cuvette, with a gradually decreasing density upwards towards the middle of the sample. The spheres are individually distinguishable throughout the lower density areas of the sample, as seen in Figs. 11(*c*) and 11(*d*).

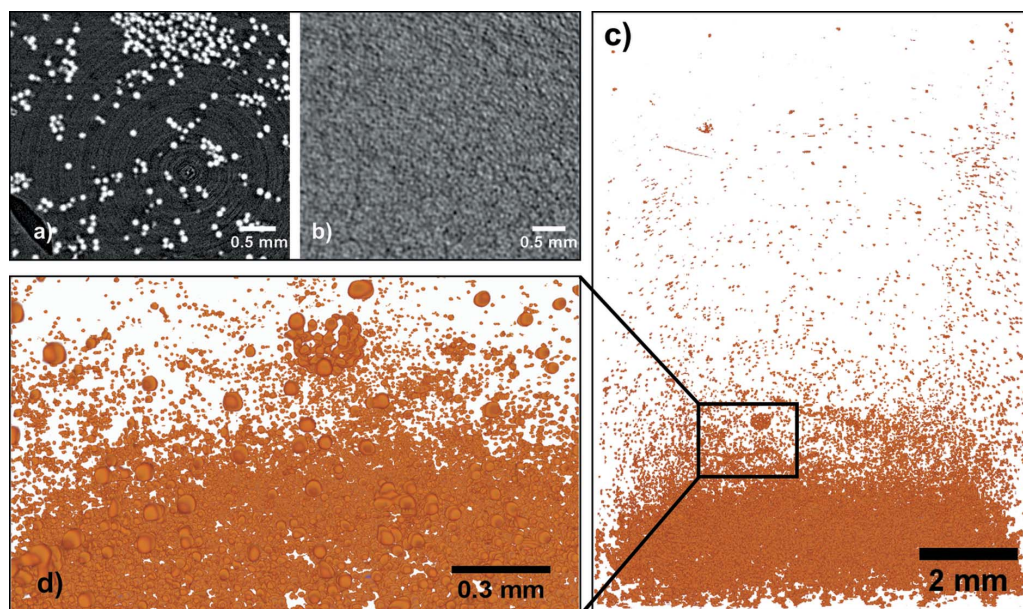


Figure 11

Area of a CT slice shown for lung phantoms of 90–106 μm solid glass spheres suspended in (a) agarose gel and (b) air. (c) 3-D rendering of the sample shown in (a), with (d) the highlighted inset in detail, with an adjusted viewing angle of 15° above the horizontal to better view the group of spheres seen near the top of the inset.

4.7. Mouse lung imaging

To test the validity of our investigations, a mouse lung was imaged *in situ*, *post mortem*, as seen in Fig. 12, using the superconducting multipole wiggler as the source. Exposure times of 50 ms and 2 s were utilized to provide both a realistic live animal imaging exposure and a low-noise image, respectively. As can be seen, the 50 ms exposure image contains significantly more noise and thus a reduced signal-to-noise ratio in comparison with the 2 s image; however, the structure of the lungs is still clearly visible and provides sufficient contrast for XV of lung motion. These images are very promising for useful *in vivo* imaging of live animal lung dynamics on the IMBL. Sample preparation was completed under animal ethics committee approvals from the Women's and Children's Health Network, the University of Adelaide and the Australian Synchrotron.

5. Conclusions

A feasibility study for imaging the lungs of small animals *via* propagation-based phase-contrast imaging at 30 keV was undertaken on the Imaging and Medical beamline at the Australian Synchrotron. Measurements of the effective source size, in both the horizontal and vertical directions, and the sample-to-detector distance were performed in the two hutches of IMBL used for phase-contrast imaging of animals, hutches 2B and 3B, at 31.7 and 135 m from the source,

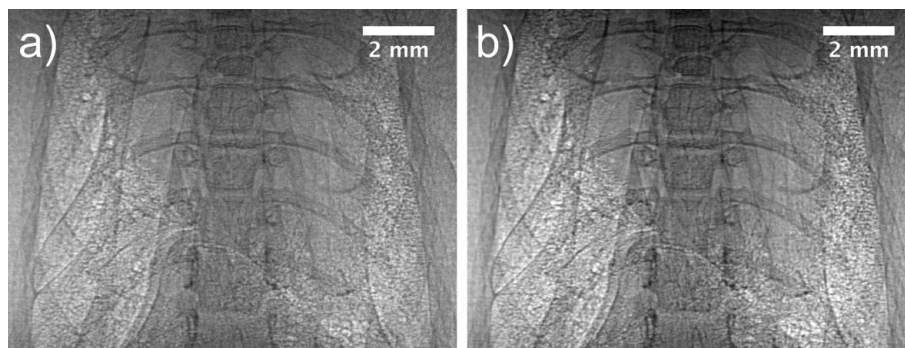


Figure 12

Mouse lung (strain C57) imaged *post mortem*. This image was obtained using the new superconducting multipole wiggler at 30 keV, $R_2 = 4$ m in hutch 3B. The exposure time was (a) 50 ms and (b) 2 s. The grey scale is the same for the two images.

respectively. It was found that a primary slit width in the horizontal direction of 2–15 mm had no significant impact on image quality or exposure time in hutch 3B; however, horizontal collimation did make a significant impact on the field of view in hutch 2B. Interestingly, increasing the vertical effective source size by bending the monochromator crystals also increased the horizontal effective source size. This may be advantageous in order to decrease the required exposure time in hutch 2B, which is a key consideration in live animal imaging.

Analysis of the sample-to-detector distance showed the benefit of the large R_2 propagation distances (up to approximately 6 m) available in hutch 3B for imaging larger objects, as seen by the high-contrast fringes produced from the 1.5 mm perspex spheres imaged at $R_2 = 5.96$ m. However, it was demonstrated that these large distances also introduce a sufficient probability of photon scatter in air with an asso-

ciated reduction in contrast and resolution. Of particular note was increased blurring in the horizontal direction in hutch 3B, the cause of which requires further investigation.

PB-PCXI of mouse lung speckle at 30 keV in hutch 2B is advised to be undertaken at 15 mm PSW, with a crystal bend in the region of 1.5. In hutch 3B, the exposure time of 2 s was too long to translate to live animal imaging; however, higher-contrast speckle images observed through a 2 mm PSW and $CB = 0$ may be translatable to imaging with the new superconducting multipole wiggler. A sample-to-detector propagation distance of between 0.5 and 3 m is preferable, and users should keep in mind that $R_2 > 3$ m may be affected by photons scattering in air. In this instance, use of a low- or non-scattering medium, such as a helium or vacuum tube, between the sample and detector to reduce scattering effects may be beneficial.

X-ray velocimetry was successfully undertaken on lung phantom speckle images. Of particular success was the phantom composed of high-packing-density 63–75 μm glass spheres in air, imaged at a sample-to-detector distance of 5.96 m. This image was affected by significant blurring from air scatter and the decrease of speckle contrast at large R_2 distances. Nevertheless, the data were successfully analysed to yield velocity measurements, demonstrating the potential for XV to be applied to phase-contrast imaging of the lungs of live animals at the IMBL in the future.

Accurate phase retrieval was also performed, demonstrating that accurate single-image phase retrieval is achievable on images obtained on IMBL with $R_2 \leq 4$ m. Single-image phase retrieval was also applied to CT data, revealing that sufficient detail to resolve alveoli-size features is achievable with small animal airways and lungs with high detail seen at a sample-to-detector distance of 1 m with the lower-packing-density glass–agarose lung phantom.

Our investigations demonstrate that the IMBL can achieve sufficient image quality for quantitative lung imaging in small animals, using propagation-based phase-contrast imaging techniques, including three-dimensional characterization *via* CT, and dynamic processes using XV. We suggest that high-resolution live animal lung imaging will be possible with the increased flux available from the superconducting multipole wiggler.

We are grateful to the National Health and Medical Research Council of Australia for funding support, the Australian Synchrotron for provision of beam time, Jeremy Brown for his help in conducting experiments and simulations, Rajeev Samarage for technical assistance, David Parsons and Martin Donnelley for experimental assistance, and Marcus Kitchen and Chris Hall for stimulating discussions on beam-line and detector characteristics. RPM is a recipient of the Australian Postgraduate Award. KSM acknowledges DECRA funding from the Australian Research Council.

References

Adrian, R. J. (2005). *Exp. Fluids*, **39**, 159–169.

- Arfelli, F., Assante, M., Bonvicini, V., Bravin, A., Cantatore, G., Castelli, E., Dalla Palma, L., Di Michiel, M., Longo, R., Olivo, A., Pani, S., Pontoni, D., Poropat, P., Presti, M., Rashevsky, A., Tromba, G., Vacchi, A., Vallazza, E. & Zanconati, F. (1998). *Phys. Med. Biol.* **43**, 2845–2852.
- Bayat, S., Le Duc, G., Porra, L., Berruyer, G., Nemoz, C., Monfraix, S., Fiedler, S., Thomlinson, W., Suortti, P., Standertskjöld-Nordenstam, C. G. & Sovijärvi, A. R. (2001). *Phys. Med. Biol.* **46**, 3287–3299.
- Beltran, M. A., Paganin, D. M., Siu, K. K. W., Fouras, A., Hooper, S. B., Reser, D. H. & Kitchen, M. J. (2011). *Phys. Med. Biol.* **56**, 7353–7369.
- Blackstone, E., Morrison, M. & Roth, M. B. (2005). *Science*, **308**, 518.
- Carnibella, R. P., Kitchen, M. J. & Fouras, A. (2013). *Opt. Express*, **21**, 19153–19162.
- Cloetens, P., Barrett, R., Baruchel, J., Guigay, J.-P. & Schlenker, M. (1996). *J. Phys. D*, **29**, 133–146.
- Cloetens, P., Ludwig, W., Baruchel, J., Van Dyck, D., Van Landuyt, J., Guigay, J. P. & Schlenker, M. (1999). *Appl. Phys. Lett.* **75**, 2912.
- Depaola, G. (2003). *Nucl. Instrum. Methods Phys. Res. A*, **512**, 619–630.
- Dubsky, S., Hooper, S. B., Siu, K. K. W. & Fouras, A. (2011). *9th International Symposium on Particle Image Velocimetry*, Kobe, Japan.
- Dubsky, S., Hooper, S. B., Siu, K. K. W. & Fouras, A. (2012a). *J. R. Soc. Interface*, **9**, 2213–2224.
- Dubsky, S., Jamison, R. A., Higgins, S. P. A., Siu, K. K. W., Hourigan, K. & Fouras, A. (2012b). *Exp. Fluids*, **52**, 543–554.
- Dubsky, S., Jamison, R. A., Irvine, S. C., Siu, K. K. W., Hourigan, K. & Fouras, A. (2010). *Appl. Phys. Lett.* **96**, 023702.
- Faffe, D. S., Rocco, P. R. M., Negri, E. M. & Zin, W. A. (2002). *J. Appl. Physiol.* **92**, 230–234.
- Fouras, A., Allison, B. J., Kitchen, M. J., Dubsky, S., Nguyen, J., Hourigan, K., Siu, K. K. W., Lewis, R. A., Wallace, M. J. & Hooper, S. B. (2012). *Ann. Biomed. Eng.* **40**, 1160–1169.
- Fouras, A., Dusting, J., Lewis, R. & Hourigan, K. (2007). *J. Appl. Phys.* **102**, 064916.
- Fouras, A., Dusting, J., Sheridan, J., Kawahashi, M., Hirahara, H. & Hourigan, K. (2009a). *Clin. Exp. Pharmacol. Physiol.* **36**, 238–247.
- Fouras, A., Kitchen, M. J., Dubsky, S., Lewis, R. A., Hooper, S. B. & Hourigan, K. (2009b). *J. Appl. Phys.* **105**, 102009.
- Giacomini, J. C., Gordon, H., O’Neil, R., Van Kessel, A., Cason, B., Chapman, D., Lavendar, W., Gmur, N., Menk, R., Thomlinson, W., Zhong, Z. & Rubenstein, E. (1998). *Nucl. Instrum. Methods Phys. Res. A*, **406**, 473–478.
- Guigay, J.-P., Zabler, S., Cloetens, P., David, C., Mokso, R. & Schlenker, M. (2004). *J. Synchrotron Rad.* **11**, 476–482.
- Gureyev, T. E., Mayo, S. C., Myers, D. E., Nesterets, Y., Paganin, D. M., Pogany, A., Stevenson, A. W. & Wilkins, S. W. (2009). *J. Appl. Phys.* **105**, 102005.
- Gureyev, T. E., Nesterets, Y. I., Stevenson, A. W., Miller, P. R., Pogany, A. & Wilkins, S. W. (2008). *Opt. Express*, **16**, 3223–3241.
- Gureyev, T. E., Nesterets, Y., Ternovski, D., Thompson, D., Wilkins, S. W., Stevenson, A. W., Sakellariou, A. & Taylor, J. A. (2011). *Proc. SPIE*, **8141**, 81410B.
- Irvin, C. G. & Bates, J. H. T. (2003). *Respir. Res.* **4**, 1–9.
- Irvine, S. C., Paganin, D. M., Dubsky, S., Lewis, R. A. & Fouras, A. (2008). *Appl. Phys. Lett.* **93**, 153901.
- Jamison, R. A., Dubsky, S., Siu, K. K. W., Hourigan, K. & Fouras, A. (2011). *Ann. Biomed. Eng.* **39**, 1643–1653.
- Jannasch, K., Missbach-Guentner, J. & Alves, F. (2009). *Drug Discov. Today*, **6**, 129–135.
- Kitchen, M. J., Lewis, R. A., Morgan, M. J., Wallace, M. J., Siew, M. L., Siu, K. K. W., Habib, A., Fouras, A., Yagi, N., Uesugi, K. & Hooper, S. B. (2008). *Phys. Med. Biol.* **53**, 6065–6077.
- Kitchen, M. J., Paganin, D., Lewis, R. A., Yagi, N., Uesugi, K. & Mudie, S. T. (2004). *Phys. Med. Biol.* **49**, 4335–4348.

- Larsson, D. H., Lundström, U., Westermark, U. K., Arsenian Henriksson, M., Burvall, A. & Hertz, H. M. (2013). *Med. Phys.* **40**, 021909.
- Lewis, R. A., Hall, C. J., Hufton, A. P., Evans, S., Menk, R. H., Arfelli, F., Rigon, L., Tromba, G., Dance, D. R., Ellis, I. O., Evans, A., Jacobs, E., Pinder, S. E. & Rogers, K. D. (2003). *Br. J. Radiol.* **76**, 301–308.
- Lewis, R. A., Yagi, N., Kitchen, M. J., Morgan, M. J., Paganin, D., Siu, K. K. W., Pavlov, K., Williams, I., Uesugi, K., Wallace, M. J., Hall, C. J., Whitley, J. & Hooper, S. B. (2005). *Phys. Med. Biol.* **50**, 5031–5040.
- Lovric, G., Barré, S. F., Schittny, J. C., Roth-Kleiner, M., Stampanoni, M. & Mokso, R. (2013). *J. Appl. Cryst.* **46**, 856–860.
- Mayo, S. C., Davis, T., Gureyev, T. E., Miller, P. R., Paganin, D. M., Pogany, A., Stevenson, A. W. & Wilkins, S. W. (2003). *Opt. Express*, **11**, 2289–2302.
- Morgan, K. S., Donnelley, M., Paganin, D. M., Fouras, A., Yagi, N., Suzuki, Y., Takeuchi, A., Uesugi, K., Boucher, R. C., Parsons, D. W. & Siu, K. K. W. (2013). *PLoS One*, **8**, e55822.
- Morgan, K. S., Irvine, S. C., Suzuki, Y., Uesugi, K., Takeuchi, A., Paganin, D. M. & Siu, K. K. W. (2010). *Opt. Commun.* **283**, 216–225.
- Ng, I., Paganin, D. M. & Fouras, A. (2012). *J. Appl. Phys.* **112**, 074701.
- NIST (2011). Physical Reference Data. NIST, Gaithersburg, MD, USA.
- Nugent, K. A. (2010). *Adv. Phys.* **59**, 1–99.
- Paganin, D. (2006). *Coherent X-ray Optics*. Oxford University Press.
- Paganin, D. M., Mayo, S. C., Gureyev, T. E., Miller, P. R. & Wilkins, S. W. (2002). *J. Microsc.* **206**, 33–40.
- Schleede, S., Meinel, F. G., Bech, M., Herzen, J., Achterhold, K., Potdevin, G., Malecki, A., Adam-Neumair, S., Thieme, S. F., Bamberg, F., Nikolaou, K., Bohla, A., Yildirim, A. Ö, Loewen, R., Gifford, M., Ruth, R., Eickelberg, O., Reiser, M. & Pfeiffer, F. (2012). *Proc. Natl Acad. Sci. USA*, **109**, 17880–17885.
- Siu, K. K. W., Morgan, K. S., Paganin, D. M., Boucher, R., Uesugi, K., Yagi, N. & Parsons, D. W. (2008). *Eur. J. Radiol.* **68**, S22–S26.
- Snigirev, A., Snigireva, I., Kohn, V., Kuznetsov, S. & Schelokov, I. (1995). *Rev. Sci. Instrum.* **66**, 5486.
- Stevenson, A. W., Hall, C. J., Mayo, S. C., Häusermann, D., Maksimenko, A., Gureyev, T. E., Nesterets, Y. I., Wilkins, S. W. & Lewis, R. A. (2012). *J. Synchrotron Rad.* **19**, 728–750.
- Stevenson, A. W., Mayo, S. C., Häusermann, D., Maksimenko, A., Garrett, R. F., Hall, C. J., Wilkins, S. W., Lewis, R. A. & Myers, D. E. (2010). *J. Synchrotron Rad.* **17**, 75–80.
- Suzuki, Y. (2004). *Rev. Sci. Instrum.* **75**, 1026.
- Suzuki, Y., Yagi, N. & Uesugi, K. (2002). *J. Synchrotron Rad.* **9**, 160–165.
- Voorhees, A., An, J., Berger, K. I., Goldring, R. M. & Chen, Q. (2005). *Magn. Reson. Med.* **54**, 1146–1154.
- Weitkamp, T., David, C., Kottler, C., Bunk, O. & Pfeiffer, F. (2006). *Proc. SPIE*, **6318**, 63180S.
- Westerweel, J. & Scarano, F. (2005). *Exp. Fluids*, **39**, 1096–1100.
- Wilkins, S. W., Gureyev, T. E., Gao, D., Pogany, A. & Stevenson, A. W. (1996). *Nature (London)*, **384**, 335–338.
- Yagi, N., Suzuki, Y., Umetani, K., Kohmura, Y. & Yamasaki, K. (1999). *Med. Phys.* **26**, 2190–2193.
- Zhou, S. A. & Brahme, A. (2008). *Phys. Med.* **24**, 129–148.